Reprinted from I&EC RESEARCH, 1990, 29, 139.

Calcination and Sintering Models for Application to High-Temperature, Short-Time Sulfation of Calcium-Based Sorbents

Corey R. Milne, Geoffrey D. Silcox, and David W. Pershing*
Department of Chemical Engineering, The University of Utah, Salt Lake City, Utah 84112

David A. Kirchgessner
Air and Energy Engineering Research Laboratory, U.S. Environmental Protection Agency, Research Triangle Park, North Carolina 27711

To simulate the staged availability of transient high surface area CaO observed in high-temperature flow-reactor data, the rate of calcination of $CaCO_3$ or $Ca(OH)_2$ is described by an empirical modification of the shrinking-core model. The physical model depicts particle decomposition by the shrinking-core mechanism. The subsequent time-dependent decrease in CaO reactivity (surface area and porosity) due to sintering is simulated by reducing the grain-center spacing for the matrix of overlapping CaO grains. Information from SEM micrographs and from other physical property measurements of the porous particles is incorporated. This submodel simulates the time-dependent availability and reactivity of CaO for a comprehensive model used to study sulfation of $CaCO_3$ and $Ca(OH)_2$ particles at upper-furnace injection conditions.

Snow et al. (1988) reported direct sulfation of $CaCO_3$ at temperatures below 1123 K,

$$CaCO_3(s) + SO_2(g) + \tfrac{1}{2}O_2(g) \rightarrow CaSO_4(s) + CO_2(g) \quad (1)$$

a reaction that is pertinent to sulfur control for fluidized-bed combustion of coal.

Dry sorbent injection in pulverized coal boilers occurs at higher temperatures (1100–1500 K). Consequently, the sorbent initially calcines before undergoing sulfation,

$$CaCO_3(s) \rightarrow CaO(s) + CO_2(g) \quad (2)$$

$$Ca(OH)_2(s) \rightarrow CaO(s) + H_2O(g) \quad (3)$$

$$CaO(s) + SO_2(g) + \tfrac{1}{2}O_2(g) \rightarrow CaSO_4(s) \quad (4)$$

A nonporous $CaCO_3$ (carbonate) or $Ca(OH)_2$ (hydrate) solid decomposes to a porous CaO solid of the same volume with porosities of 54% and 49%, respectively. The porosity differences are due to the inequality of the molar volumes. At the elevated temperatures of interest, sintering of the solid reduces the surface area and porosity developed in the calcination process. Because $CaSO_4$ has a higher molar volume than CaO by a factor of 2.72, sulfation of the porous CaO reduces and probably in time blocks the pore volume of the particle.

Small carbonate or hydrate particles dispersed in a high-temperature gas flow reactor with SO_2 present experience rapid initial sulfation with lower reaction rates at longer times, Figure 1. When compared to the calcination data of Borgwardt (1985) that show 90% calcination in <0.25 s for 10-μm limestone particles at 1348 K, it is apparent that initially decomposition and sulfation reactions occur simultaneously.

The sulfation of porous CaO particles consists of reaction at the CaO surface (extremely rapid), solid-state diffusion through the $CaSO_4$ product layer, and pore diffusion of SO_2 through the particle. All three of these processes are directly related to the structural properties of the CaO particle. To model the high-temperature, short-time sulfation of $CaCO_3$ and $Ca(OH)_2$ particles at boiler injection conditions, the particle structure and the time dependent of CaO availability and reactivity, controlled by calcination and sintering, must be incorporated.

A number of structural models have been applied in the area of noncatalytic gas–solid reactions. Ramachandran and Doraiswamy (1982), Lindner and Simonsson (1981), and Szekely et al. (1976) reviewed the different models. In principle, most of the models simulate the porous particle as a sphere composed of small spherical grains or cylindrical pores. More sophisticated models incorporate a distribution of grain or pore sizes. Lindgren (1988) viewed the particle as a composition of concentric shells with a separate pore size distribution for each shell. Silcox et al. (1989) modeled the calcination process with a shrinking-core mechanism that produces spherical shells of CaO that subsequently sinter at independent rates.

The structural parameters for these models are often set from calculated surface areas and pore volumes based on nitrogen adsorption and mercury penetration measurements. Particle size is determined by sieve analysis for >100-μm particles. For smaller particles, Stoke's law settling or Coulter counter techniques are employed. SEM micrographs provide qualitative as well as quantitative information about the structure of the particle.

This paper described the results of a combined experimental and theoretical study to develop an activation model for calcium-based sorbents. The model was formulated based on detailed examination of SEM micrographs; it assumes that decomposition (to CaO) occurs by

* Author to whom all correspondence should be addressed.

0888-5885/90/2629-0139$02.50/0

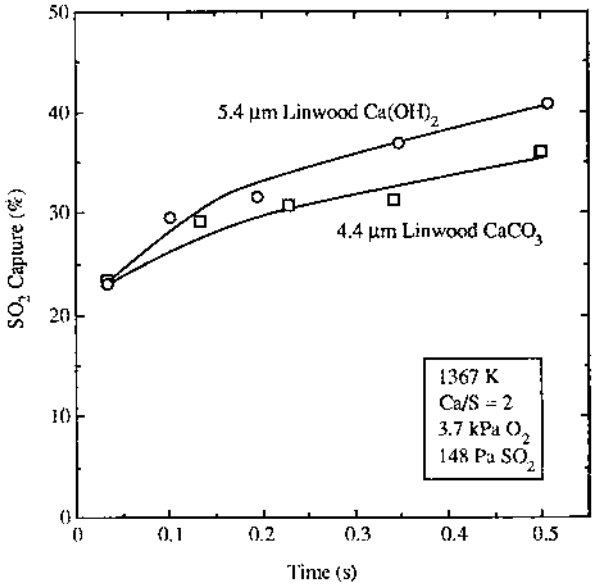

Figure 1. Laboratory sulfation rate data from a 30-kW dispersed-phase isothermal reactor (Milne, 1988).

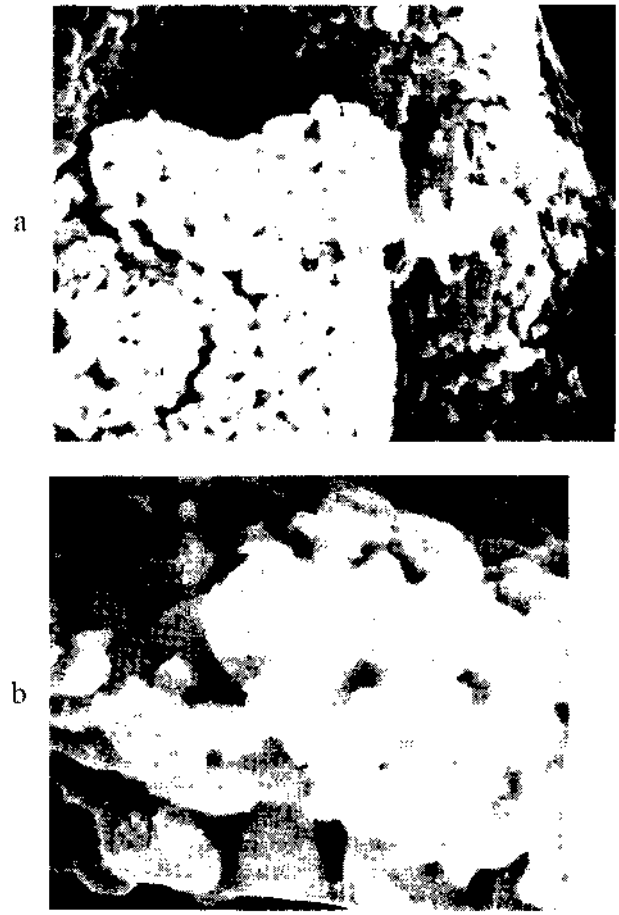

Figure 2. SEM photomicrograph of 8.9-μm Linwood carbonate, calcined at 1073 K in a 5-mm-deep ceramic dish for (a) 45 min and (b) 16 h (1.8 cm = 1.0 μm).

a modified shrinking-core mechanism. The subsequent time-dependent decrease in CaO reactivity (due to sintering) is simulated by reducing the grain-center spacing for the matrix of overlapping CaO grains.

Structural Model for CaO

SEM Data. Figure 2a shows the structure of a CaO particle produced from calcination of 8.9-μm Linwood carbonate at 1073 K in a 5-mm deep ceramic dish in an air-purged electric muffle furnace. The appearance is very similar to that reported by Borgwardt and Harvey (1972). Note the presence of necks that join the nonuniform grains together in a continuous matrix. The pores are tortuous and asymmetric.

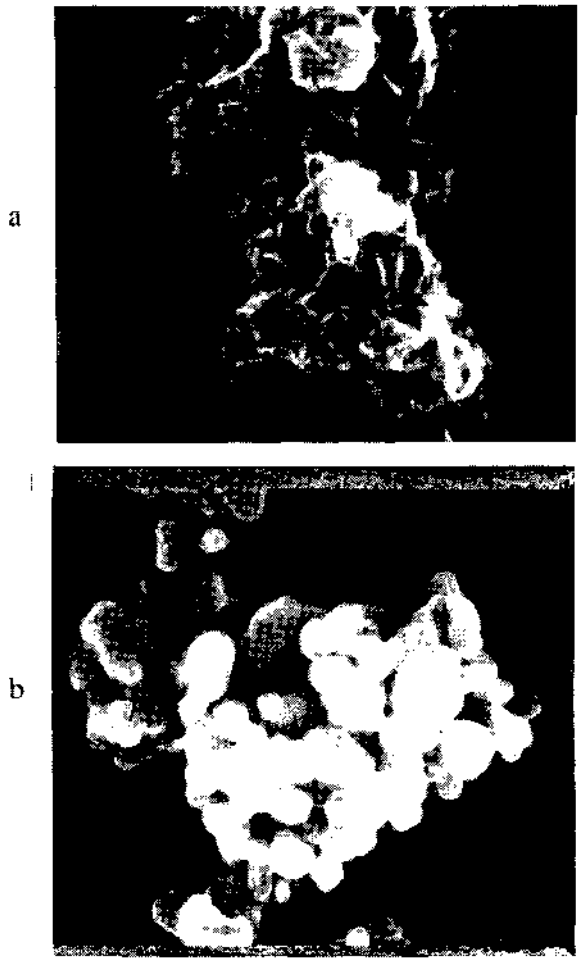

Figure 3. SEM photomicrograph of 5.4-μm Linwood hydrate, calcined in a 5-mm-deep ceramic dish at (a) 973 K for 8 min and (b) 1073 K for 6 h (1.8 cm = 1.0 μm).

Figure 2b shows the same CaO after an additional 15.25 h of sintering at 1073 K. The larger grain size in this highly sintered sample corroborates nitrogen adsorption data that indicate a decrease in surface area from 11 to 3.7 m^2/g and a decrease in porosity from 21% to 2.8%. The equivalent spherical grain diameters for these two BET surface areas are 0.16 and 0.49 μm, respectively.

Figure 3 reveals the influence of sintering on a 5.4-μm Linwood hydrate calcined at 973 K for 8 min and at 1073 K for 6 h. The long-term heating reduced the surface area from 21 to 3.9 m^2/g (an increase in equivalent spherical grain diameter from 0.086 to 0.46 μm) and reduced the porosity from 23% to 4.5%.

The CaO of Figure 3b appears to have more than 4.5% void volume. The pore volume determination by nitrogen adsorption for these samples, as measured with a Micromeritics Digisorb instrument, has limited accuracy for low surface area solids or for solids with a significant number of pores larger than 600 Å. The vapor pressure is not significantly affected by the larger radii of curvature for large pores (Smith, 1981). This technique, along with mercury intrusion, for determining internal pore structure dimensions is very reliable for evaluating relative differences or changes, but the accuracy of the absolute number is a function of how close the model used for the calcula-

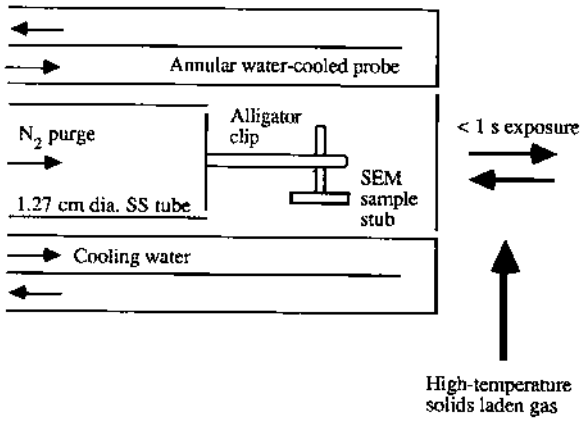

Figure 4. Sample probe used to collect solids entrained in a high-temperature gas flow stream for SEM observation.

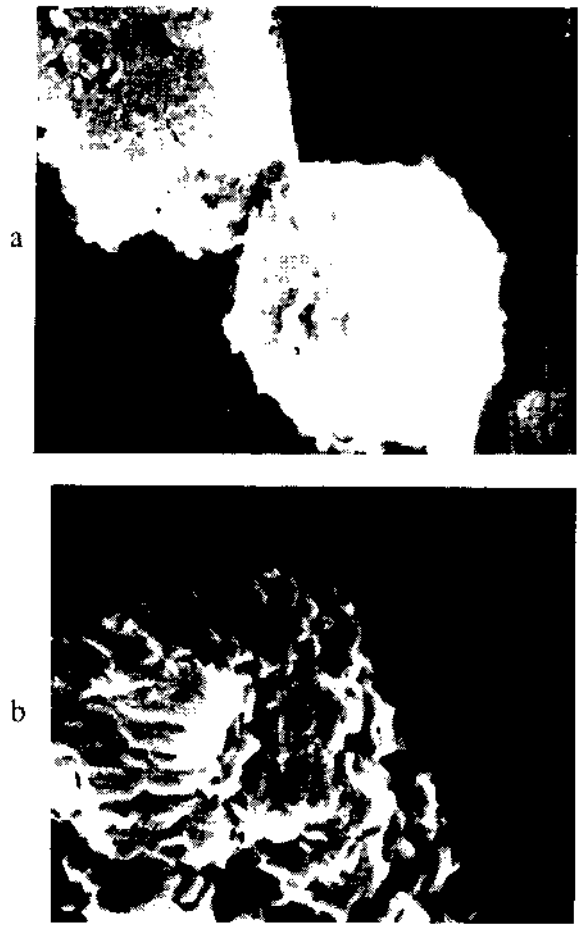

Figure 5. SEM photomicrograph of 4.4-μm Linwood carbonate, calcined at 1367 K in an isothermal flow reactor for (a) 35 ms and (b) 500 ms (1.8 cm = 1.0 μm).

tions matches the actual physical features of the solid.

The structures of the high surface area CaO from the two parent stones, Figures 2a and 3a, are substantially different. These dissimilar structures support the low-temperature (<1100 K) findings of Gullett and Bruce (1987) and Beruto et al. (1980). They reported that characteristics of the nitrogen adsorption isotherms suggest that CaO produced from the carbonate (c-CaO) has a cylindrical pore structure, while CaO derived from hydrate (h-CaO) is better represented as having slit- or platelike pores.

Samples of CaO decomposed under high-temperature, short-time conditions (>1200 K, <1 s) similar to that observed in upper furnace sorbent injection are difficult to

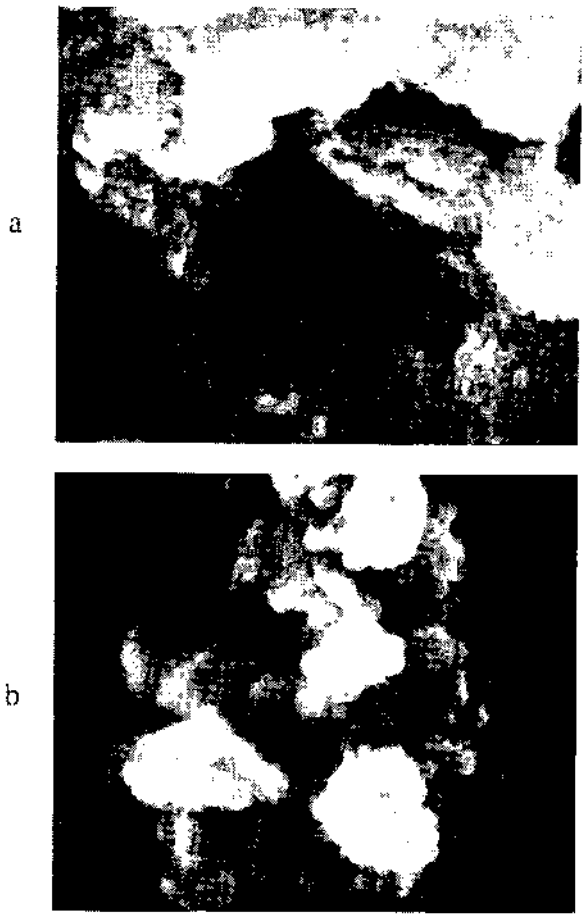

Figure 6. SEM photomicrograph of raw Linwood hydrate, calcined in an isothermal flow reactor at 1367 K for (a) 35 ms and (b) 500 ms (1.8 cm = 1.0 μm).

obtain without compromising the solid with the sampling procedure. Gathering the CaO particles in a dispersed-phase reactor usually entails a high-temperature collection system that rapidly cools the sample to a temperature that will avoid condensation of the water vapor and prevent further decomposition and sintering. Unfortunately, the light loading of the solids in the gas phase necessitates prolonged sample times of several minutes to gather sufficient solids for analysis. During that sample period, the highly reactive CaO can partially react with CO_2 and H_2O in the gas passing over the sample solids to form $CaCO_3$ and $Ca(OH)_2$, respectively (Bortz and Flament, 1985).

To determine whether the CaO produced at low temperatures is representative of that found under sorbent injection conditions, a method was devised to sample an extremely small amount of CaO directly from a high-temperature reactor with minimal alteration of the solid by the sampling procedure. The apparatus is illustrated in Figure 4. The very adhesive CaO particles were collected directly on the surface of a highly polished aluminum SEM sample stub. A dry nitrogen purge prevented flue gas from flowing up the sample probe and compromising the highly reactive CaO solids. An exposure time of less than 1 s in a 1367 K solid-laden gas stream produced a negligible temperature increase of the aluminum stub and deposited an almost invisible dusting of <10-μm CaO particles on the surface of the sample stub. The sample was subsequently coated with a gold–palladium alloy for SEM observation.

Figures 5 and 6 are SEM photomicrographs of samples extracted in this manner from a 1367 K dispersed-phase isothermal reactor at solid reaction times of 35 and 500

ms. These solids have significantly different structures than observed in the low-temperature CaO of Figures 3 and 4.

The 35-ms c-CaO of Figure 5a has less apparent porosity than expected for an extent of decomposition of 50%, based on predicted values from the calcination model developed subsequently in this article. The surface appears granular, but the interior porosity is not visible. Note the uneven cracks possibly induced by the shock heating of the particle. The 500-ms c-CaO of Figure 5b shows considerable glazing of the surface due to sintering.

The h-CaO photomicrographs of Figure 6 show a more granular structure with a higher apparent porosity. At 35 ms, the 2.5-μm hydrate particles are fully calcined, by calcination model predictions. Throughout this work, the term grain is used in reference to the small units of solids that as a body constitute the larger, porous particle. The 500-ms grains appear to be larger than the 35-ms grains, possibly due to sintering.

From these SEM photomicrographs, it was concluded that the low-temperature, fixed-bed calcination CaO is not representative of that produced under rapid heating, high-temperature calcination conditions. The basic structure of porous CaO appears to be a matrix of interconnected grains.

Model Concept. The individual, noncontacting spheres of a simple grain model are inadequate to represent this CaO structure. A pore model is inappropriate because the particle structure is better described as a matrix of interconnected grains rather than a solid perforated with cylindrical pores.

Lindner and Simonsson (1981) represented this type of structure with a model of overlapping spheres. A simple grain model with uniform spheres cannot realistically account for a porosity of less than 26%, the void fraction of a face-centered packing of spheres, unless grain overlap is ignored. A grain model with a distribution of grain sizes is necessary to represent lower porosities. In addition to its ability to model low porosities with a single grain diameter, the overlapping grain model also represents the fact born out by SEM data: not all surfaces of the grain are in contact with the gas phase.

Kingery and Berg (1955) explained that sintering of two spheres may occur by the centers of the spheres approaching and the resultant overlapping volume filling the neck volume between the spheres. This mechanism accounts for loss of surface area and shrinkage. Coble (1958) suggested a modification where the excess volume between the spheres is redistributed to the entire free surface rather than just the neck region. This mechanism results in a simpler mathematical treatment and was subsequently applied to the overlapping grain model.

A nonoverlapping grain model simulates the grain growth shown in Figure 2 by combining small grains of high surface area to produce fewer large grains with low surface area. However, this mechanism cannot represent the associated shrinkage for porosities of less than 26%. A distributed grain size model preferentially combines small grains to form large grains, thus reducing its ability to accurately represent a low-porosity CaO and conceivably causing porosity to increase as the surface area decreases. The overlapping grain model simulates sintering by moving the grain centers closer together, resulting in concurrent surface area and porosity reduction.

Mathematical Development. As shown in Figure 7, a single grain is viewed as a sphere with a fraction of its exterior cut away to represent the interface with a neighboring sphere. If a plane passes through a sphere of radius

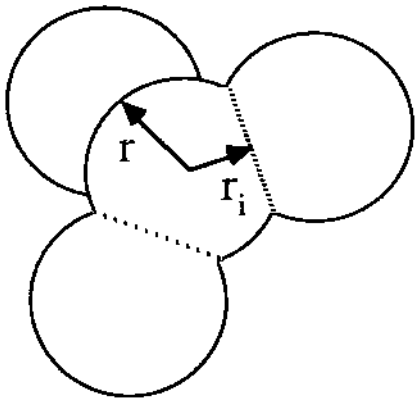

Figure 7. Illustration of the overlapping grain model.

r at a perpendicular distance r_i from the center, the surface area and volume of the segmented portion of the sphere (Eves, 1978) are, respectively,

$$S_o = 2\pi r^2\left(1 - \frac{r_i}{r}\right) \tag{5}$$

$$V_o = \frac{\pi}{3}r^3\left[2 - 3\frac{r_i}{r} + \left(\frac{r_i}{r}\right)^3\right] \tag{6}$$

If two spheres overlap, each sphere will have a surface area and volume reduced by the values of eqs 5 and 6, respectively. In a system of overlapping spherical grains with n contacts per grain, the grain surface area and volume are

$$S_g = 4\pi r^2\left[1 - \frac{n}{2}\left(1 - \frac{r_i}{r}\right)\right] \tag{7}$$

$$V_g = \frac{4}{3}\pi r^3\left\{1 - \frac{n}{4}\left[2 - 3\frac{r_i}{r} + \left(\frac{r_i}{r}\right)^3\right]\right\} \tag{8}$$

These two equations describe the grain structure as introduced by Lindner and Simonsson (1981) by including the number density of grains, N,

$$S = NS_g \tag{9}$$

$$1 - \epsilon = NV_g \tag{10}$$

where S is the surface area per particle volume and ϵ is the porosity. Substitution of eqs 7 and 8 into eqs 9 and 10 yields a system of two equations and six variables. The variables ϵ, S, N, and n are specified to solve for r and r_i. The nonlinear system of equations is solved by the Newton–Raphson method.

Evaluation of these variables from actual measurements is practical only for the extensive properties of surface area and porosity. For dimensions taken from SEM photomicrographs to be representative, a large number of particles must be sampled, and the exterior properties of the solid must be assumed constant throughout the interior that is not visible.

Figure 8 shows the coordination number and porosity for various spherical packings. For overlapping spheres, the maximum value of n is also 12. To be compatible with regular spherical packings, the curve drawn in Figure 8 is used to specify the coordination number of the overlapping grain model for a given porosity:

$$n = \begin{cases} 12, & \text{for } \epsilon \le 0.26 \\ 27.64\exp(-3.209\epsilon), & \text{for } \epsilon > 0.26 \end{cases} \tag{11}$$

Prior to sintering, the configuration of the overlapping grain model is taken to be almost identical with that of

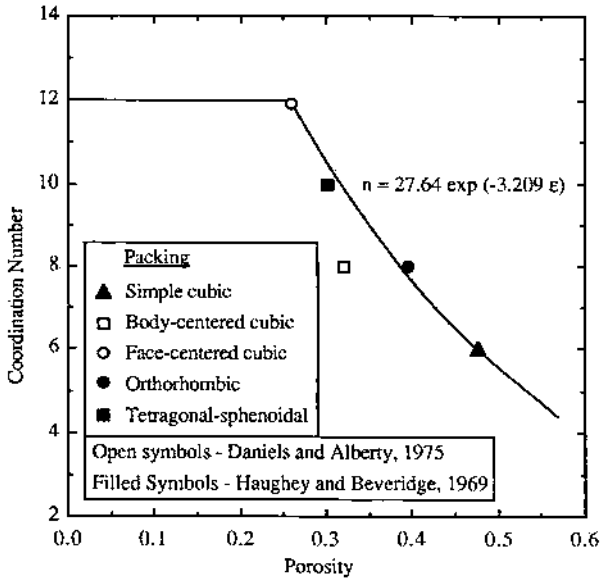

Figure 8. Coordination number as a function of porosity for the overlapping grain model based on regular spherical packings.

the grain model for porosities greater than 26%. Initially, the interface radius ratio, R_0, for a CaO grain is calculated with

$$R_0 = \begin{cases} 0.99, & \text{for } n < 12 \\ 0.8333 + 0.6026\epsilon, & \text{for } n = 12 \end{cases} \quad (12)$$

where $R_0 = r_i/r_0$

An R_0 value of 1.0 is avoided because some of the partial derivatives of eqs 7 and 8 are undefined at that point. Equation 12 accounts for the fact that the grain surface area approaches zero when the interface radius approaches a minimum value,

$$(r_i/r)_{min} = 1 - 2/n \quad (13)$$

Application of the relationship between the surface area per volume of the particle and the surface area per mass of the solids,

$$S = \rho S_m(1 - \epsilon) \quad (14)$$

and combination of eqs 9 and 10 to eliminate N yield an equation for the initial overlapping grain radius,

$$r_0 = \frac{3\left[1 - \frac{n}{2}(1 - R_0)\right]}{\rho S_m\left[1 - \frac{n}{4}(2 - 3R_0 + R_0^3)\right]} \quad (15)$$

Subsequently, r_i is determined from eq 12, and substitution of eq 8 into eq 10 yields the initial value of N.

Sintering Model

The sintering of grains at high temperatures is driven by capillary forces associated with the curvature of the surfaces (Fischer, 1955b). By diffusion or viscous flow processes, material is transferred to the high surface area regions in the granular structure, primarily the grain neck area. The sintering process influences two features of the particle structure, surface area and porosity. Because of the strong influence of these two properties on the rate of sulfation of CaO, it is desirable to quantify the change in porosity and surface area through the sintering process.

Fundamental understanding of the sintering of CaO under sorbent injection conditions is inadequate to provide a reliable theoretical model of the process. Therefore, the sintering model developed herein is based on a consistent set of empirical relations that mathematically describe trends in the available fundamental data. Derivation of the model is specific to small particles in a dispersed phase typical of dry sorbent injection.

Surface Area Loss. Sintering of CaO grains is often quantified by measurement of surface area loss with time as a function of the temperature and concentration of the gas species that catalyze sintering (CO_2 and H_2O). It is commonly accepted that increased temperature or increased CO_2 and H_2O concentrations accelerate the rate of loss of the surface area (Borgwardt et al., 1986; Mai, 1987). Newton (1987) reported that sintering is also promoted by the presence of SO_2.

German and Munir (1976) developed a rate equation based on the theory that sintering is driven by the curvature gradient at the necks of contacting grains. Borgwardt (1988, 1989) analyzed differential reactor sintering data with this rate equation. The German and Munir model fit the data well with two adjustable parameters. However, a fundamental premise of the model is that the grain necks are isolated, a condition that is violated when necks merge for surface area reductions greater than 50%. Sintering of CaO often results in much lower reductions in the surface area. A curious feature of the model is that the rate of sintering is a function of the initial surface area before sintering commenced. Therefore, this model predicts that a 50 m^2/g CaO with an initial surface area of 100 m^2/g will sinter at a different rate than a 50 m^2/g CaO with an initial surface area of 60 m^2/g. Data to support or discount this characteristic are not available. An objectionable feature of the differential form of the German and Munir rate equation is that the sintering rate is infinite at time zero.

In keeping with the theory that sintering is a physical transformation to lower surface energy, Nicholson (1965) proposed that the rate of surface area loss is proportional to the difference between the actual surface area and the equilibrium surface area that the particle reaches after long sintering times. Silcox et al. (1989) used the square of this surface area difference to correlate the rate data of Borgwardt et al. (1985) as a function of temperature and partial pressure of CO_2. An equilibrium or asymptotic surface area of 5 m^2/g was used for high temperatures because this value approximates the surface area of highly sintered materials (Borgwardt, 1988). The overall fit was not found to be very sensitive to this value.

The Silcox rate equation is modified to correspond with recent data of Borgwardt (1988) that include the influence of H_2O as well as CO_2:

$$dS_m/dt = -2450(1 + 50.7p_{H_2O}^{0.17} + 10.3p_{CO_2}^{0.67}) \exp(-29600/T)(S_m - 5000)^2 \quad (16)$$

The partial pressure of H_2O and CO_2 (kilopascals) included in the preexponential term reflects the observation in Figure 9 that sintering atmospheres containing these two gases result in higher sintering rates than measured in pure N_2. The rate constants for sintering in atmospheres containing N_2 mixed with either H_2O or CO_2 at 1073 K were evaluated for H_2O partial pressures of 0, 0.39, 7.31, and 15.2 kPa and CO_2 partial pressures of 0, 0.102, 1.02, and 12.2 kPa, respectively. As shown in Figure 9, the two rate constants for CO_2- and H_2O-catalyzed sintering are additive for predicting the rate constant for a mixture of CO_2, H_2O, and N_2.

A correlation of the rate constants for 12.2-kPa CO_2 sintering data (Borgwardt, 1988) at 1073, 1341, and 1389 K is the basis for the preexponential value, 2450 kg/(m^2

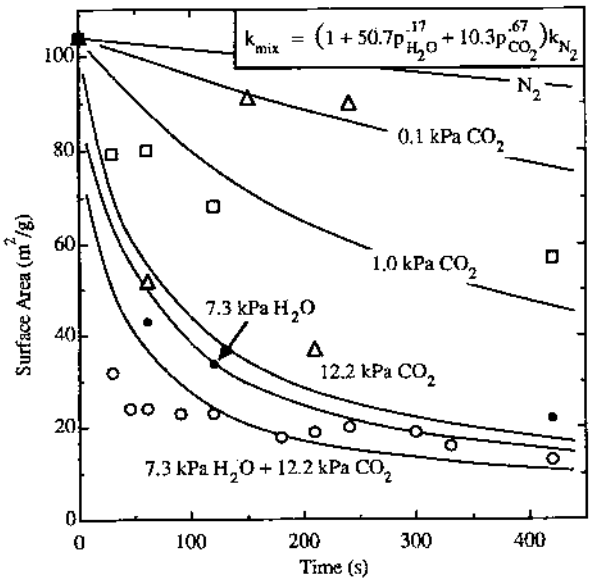

Figure 9. Comparison of 1073 K sintering data from Borgwardt (1988) with model fit of sintering rate constant in gas mixtures of carbon dioxide, water vapor, and nitrogen.

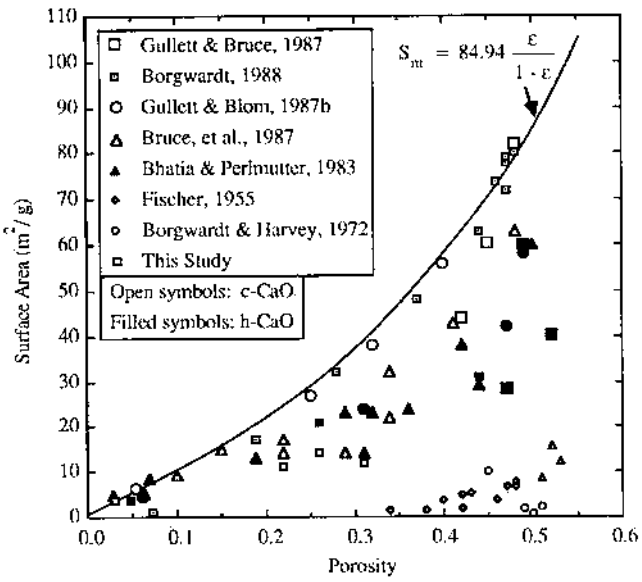

Figure 10. Surface area and porosity measurements for hydrate and carbonate derived CaO with differing degrees of sintering and varying calcination conditions.

s), and the activation energy, 29.6 kcal/mol. Sintering data (Borgwardt, 1989) for a N_2 atmosphere at 1173, 1223, and 1273 K yield a similar activation energy of 30.3 kcal/mol, implying that the influence of CO_2 and H_2O are properly included in the preexponential term of the rate constant. Sintering data at sorbent injection conditions are sparse, so eq 16 is used to extrapolate sintering rates to those conditions.

The numerical integration of eq 16 for nonisothermal conditions experienced in sorbent injection is much simpler than that of the German and Munir model.

For low mole fractions, <1%, a small increase in CO_2 or H_2O partial pressure results in a large increase in the sintering rate. However, the sintering rate appears to approach an upper limit as the concentration is increased. There are no data that show the sintering rate at concentrations approaching pure CO_2 or H_2O to assist in modeling the sintering of CaO in the interior of a decomposing particle of $CaCO_3$ or $Ca(OH)_2$ where locally high concentrations of the product gas occur.

For lack of fundamental rate data, the contention of Newton (1987) that SO_2 catalyzes sintering is not included in the sintering rate equation. For application of eq 16 to a sulfation environment, it is assumed that the sintering rate of CaO grains covered with a product layer of $CaSO_4$ is equal to that of unsulfated CaO.

Porosity Loss. Not all types of sintering induce shrinkage. The mechanisms of evaporation–condensation and surface diffusion do not reduce the porosity of the particle during sintering (Kingery and Berg, 1955). Most solids sinter by grain boundary diffusion or volume diffusion, both of which cause shrinkage (Szekely et al., 1976).

The influence of sintering on CaO porosity is less quantified and less understood than the effect on CaO surface area. There are apparent discrepancies in the literature regarding the change in porosity from sintering. Nicholson (1965) stated that sintering of porous solids produced from decomposition results in the loss of surface area, but particle shrinkage is limited. Fischer (1955a) reported that limestone calcined under mild temperatures (1200–1250 K) produced a very porous CaO that could not be densified further by subsequent firing at 1580 K. In contrast, he found that, with high-temperature calcination and uninterrupted firing, porosity decreased with increased temperature. Borgwardt (1989) produced high surface area CaO from limestone calcined at 970 K that showed a reduction in both surface area and porosity at subsequent sintering temperatures between 1170 and 1370 K.

Coble (1961) showed that the density of alumina compacts is a logarithmic function of sintering time. Borgwardt (1989) used Coble's logarithmic law to model porosity data for sintered CaO as a function of time and temperature. Specific surface area and porosity were both shown to be temperature dependent, but no functional relationship between the two properties was developed.

Bhatia and Perlmutter (1980) developed a relation between surface area and porosity where the internal structure of a particle is modeled as overlapping cylinders. This approach was not specifically applied to the modeling of the sintering process.

To quantify the simultaneous loss of surface area and porosity, measurements of c-CaO and h-CaO generated under various calcination and sintering conditions have been compiled in Figure 10. There is a clear difference in the c-CaO and h-CaO data. The porosity of Linwood carbonate and hydrate was measured by mercury penetration to be 4% and 15%, respectively. The fact that the initial porosity of a hydrate could be 5 times higher than that of a carbonate accounts for some of the shift to the right of the h-CaO data in Figure 10. It is difficult to control the experimental conditions that influence h-CaO surface area conservation during the calcination process because of the rapid, low-temperature calcination of hydrate particles relative to the more manageable high-temperature carbonate calcination (Gullett and Bruce, 1987).

Another point of interest is the broad range of c-CaO surface areas measured for a single porosity. The samples that show high porosity and low surface area were produced by Bhatia and Perlmutter (1983), Borgwardt and Harvey (1972), and Fischer (1955a) from limestone particles sized at 100, 1100, and 1300 μm, respectively. The high surface area c-CaO of Borgwardt (1988) and Gullett and Bruce (1987) were produced with less than 3-μm particles in a fixed-bed reactor that greatly reduced CO_2 and H_2O diffusion limitations and thereby reduced catalyzed sintering (Borgwardt et al., 1986).

As evidenced by the low area-to-volume ratio (or large pore diameter) of the bed-calcined c-CaO of Figure 2 and

Table I. Particle Shrinkage for Sintered Linwood c-CaO and h-CaO

parent sorbent			CaO		
type	d, μm	ϵ	d, μm	ϵ	d_{calc}, μm
$Ca(OH)_2$	5.4	0.15	3.8	0.23	4.4
$Ca(OH)_2$	5.4	0.15	3.0	0.04	4.1
$CaCO_3$	4.4	0.04	4.1	0.24	3.7
$CaCO_3$	4.4	0.04	3.5	0.03	3.4
$CaCO_3$	8.9	0.04	7.1	0.29	7.6
$CaCO_3$	8.9	0.04	6.7	0.03	6.8

the large particle calcination studies (Fischer, 1955a; Borgwardt and Harvey, 1972; Bhatia and Perlmutter, 1983), the most reliable estimate of the initial surface area and porosity for small-particle c-CaO produced in a dispersed calcination reaction should be extrapolated with the data from the experimental procedure that minimizes CO_2 diffusion limitations. A large-particle calcine or CaO produced in a thick bed experiences a range of calcination and sintering conditions that render extrapolation back to the initial CaO surface area impossible. The large pore diameter of calcines generated in a locally high CO_2 environment is consistent with the findings of Ulerich et al. (1978). They reported that calcination in a 15% CO_2 atmosphere produced larger pore diameter CaO than decomposition in N_2.

Much of the Figure 10 data were obtained by sintering the same high surface area CaO for various times to achieve a range of surface areas and porosities. The sintering paths of the different data sets are not the same, indicating that the sintering process is sensitive to the conditions of the experiment and to the initial surface area and porosity. As discussed earlier, the sintering of CaO is governed by a combination of multiple processes that influences the change in surface area relative to the change in pore volume.

The vacuum calcination experiments of Beruto et al. (1980) produced 89 m^2/g c-CaO at 593 K and 133 $m^2/(g\ h)$ CaO at 853 K. Borgwardt (1988) reported 128 $m^2/(g\ h)$ CaO produced at 643 K. Borgwardt (1989) also reported average surface areas from calcination at 973 K in a N_2 atmosphere of 8 different h-CaO samples of 77 m^2/g and 12 different c-CaO samples of 104 m^2/g.

The upper limit of the CaO surface area versus porosity data of Figure 10 is taken to be the sintering path of small-diameter c-CaO calcined in a dispersed phase. For the theoretical porosity of 54%, the initial small-diameter c-CaO surface area, immediately following calcination, is extrapolated from the upper limit data of Figure 10 to be 100 m^2/g. With the lack of consistent high surface area h-CaO measurements, h-CaO is assumed to have the same initial surface area as c-CaO. Therefore, the initial surface area of small-diameter CaO produced in a dispersed environment is taken to be 100 m^2/g.

If surface area per particle volume, S, is plotted against porosity, the sintering path of many of the data sets in Figure 10 lies on a line through the origin. Also, the upper limit of the data is represented by a line instead of a curve. Therefore, a fundamental assumption of the sintering model is that $\Delta\epsilon$ is proportional to ΔS:

$$\epsilon_2 = \epsilon_1 - (\epsilon_1/S_1)(S_1 - S_2) \tag{17}$$

This assumption accounts for CaO of differing surface area to pore volume ratios, m, following different sintering paths, as observed in Figure 10. The specific surface area at some point along a single sintering path is

$$S_m = \frac{m\epsilon}{\rho(1-\epsilon)} \tag{18}$$

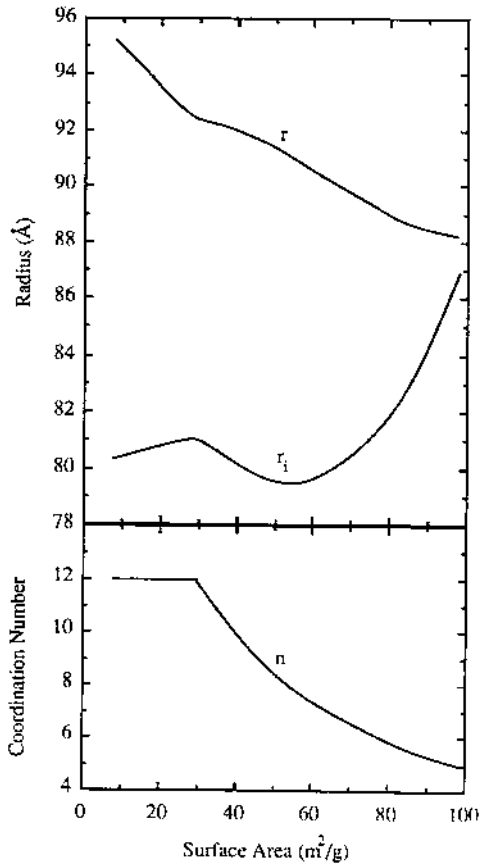

Figure 11. Changing values of r, r_i, and n for sintering of 100 m^2/g of grain.

Of course, loss of porosity equates to particle shrinkage. Table I shows measured particle diameters for sized sorbents and their calcines after various sintering times. The calculated CaO particle diameter is determined from the initial and theoretical calcine porosities of the parent sorbent and the measured CaO porosity. Mass mean particle diameters were determined by X-ray detection of the Stoke's law settling rate with a Micromeritics sedigraph.

Solution Scheme. Equation 16 is integrated to evaluate the change in specific surface area, S_m, for a single time step. The resultant loss of porosity is determined with eq 17. With eq 14, the value of S is determined, and with eq 11, the value of n is updated. With the new porosity and conservation of grain volume, V_g, through the sintering process, eq 10 yields the number density, N. Subsequently, the grain surface area, S_g, is evaluated with eq 9. The Newton–Raphson method is applied to simultaneously solve eq 7 and 8 for r and r_i.

Figure 11 shows how n, r, and r_i change as the surface area of a 100 m^2/g of CaO grain sinters to 10 m^2/g. There is a steady increase in the grain radius and coordination number (to a maximum value of 12 for face-centered cubic packing) as the surface area decreases. The interface radius, r_i, has an unexpected increase for a short period of the sintering process. The surface area of an overlapping grain of constant volume is reduced by increasing n or by decreasing r_i or by a combination of the two, which is the mechanism chosen for the sintering model. In order for the coordination number to correspond to the characteristics of regular spherical packing, Figure 8, n is set and r_i is calculated. Alternatively, r_i could be constrained to steadily decrease as the surface area decreases and r and n could then be solved for. However, this route is less stable numerically and is further removed from the body

Table II. Shrinking-Core Model Rate Constant at 983 K (Borgwardt, 1985)

S_{m0}, m^2/g	k', 10^{-8} m/s	S_{m0}, m^2/g	k', 10^{-8} m/s
0.1	3.23	1.4	1.21
0.20	3.14	7.2	0.82

of information available for packed spheres.

Calcination Model

Carbonate Rate Equation. Borgwardt (1985) measured calcination rates of $CaCO_3$ particles with narrow size distributions ranging from 1 to 90 μm in diameter. A differential fixed-bed reactor was used for temperatures of less than 1000 K and reaction times greater than 1 s. A dispersed-phase isothermal flow reactor was employed for short reaction times (0.1–0.7 s) and high temperatures (1050–1350 K), conditions necessary to simulate boiler injection.

Borgwardt showed that the instantaneous rate of calcination in the differential reactor is proportional to the initial surface area and to the fraction of remaining $CaCO_3$. Data from Snow (1985) and the theoretical calcination model of Silcox et al. (1989) accounting for CO_2 diffusion limitations indicate that carbonate calcination is kinetically controlled with negligible pore-diffusion limitations for these experimental conditions.

The classic shrinking-core model for mathematically representing a decomposition reaction is based on the assumption that the rate of change of volume of the unreacted solid is proportional to the surface area of the unreacted spherical core:

$$dV_c/dt = -k'4\pi r_c^2 \tag{19}$$

Noting that

$$V_c = (1 - x)\frac{4}{3}\pi r_0^3 \tag{20}$$

and

$$1 - x = (r_c/r_0)^3 \tag{21}$$

integration of eq 19 yields (compare Smith (1981))

$$\frac{k'}{r_0} = \frac{1 - (1 - x)^{1/3}}{t} \tag{22}$$

This model can be applied to the calcination of $CaCO_3$ by assuming that the porous carbonate particle is composed of smaller grains of $CaCO_3$ of equal diameter that calcine at equal rates. The initial surface area of the solid provides an estimate of r_0, for this case, the initial radius of the grains within the particle:

$$r_0 = \frac{3}{\rho S_{m0}} \tag{23}$$

Table II lists values of k' calculated with eq 22 for the 983 K rate data of Borgwardt (1985) plotted in Figure 12. From these values of k', it appears that application of the shrinking-core model, eq 22, to the calcination of carbonate particle grains, the radius of which is determined from the initial specific surface area of the solid, does not yield a rate constant that is independent of surface area.

Satterfield and Feakes (1959) concluded from microscopic observation of the decomposition of calcite crystals that the calcination region is a complex zone. They described the formation of cracks in the decomposing crystal that increased the surface area of reaction. This mechanism would result in an increase in k' with time. The constant values with time of the data plotted in Figure 12 do not support the possibility of increasing the surface from fragmentation as calcination proceeds.

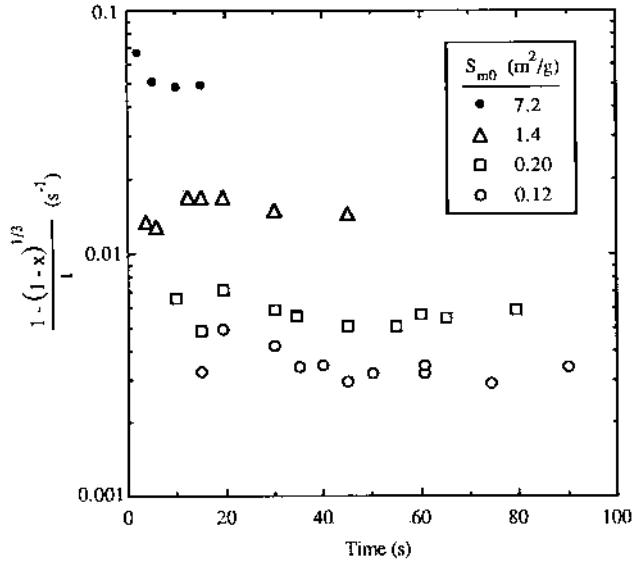

Figure 12. Differential reactor calcination rate data at 983 K from Borgwardt (1985) for various surface area carbonates.

The fundamental mechanisms governing this decomposition process are obviously more complex than portrayed by the shrinking-core model applied to the grain level of the carbonate particle. This model provides a reasonable description of the trends in the data but does not provide a satisfactory statistical fit. To study the influence of calcination on the sulfation of CaO in a comprehensive model, a more empirical approach is adopted. A calcination submodel that fits the calcination data avoids uncertainty that may arise when interpreting the sulfation model results, which include the influence of calcination.

Furthermore, the assumption that calcination occurs by a shrinking-core mechanism on the individual grains of the carbonate particle requires a simultaneous sulfation model to account for two levels of CaO within the particle. First, each grain is composed of multiple spherical shells of CaO with different exposure times after calcination, resulting in a range of surface areas (reactivity). Second, grains at different radii in the particle sulfate at different rates due to the SO_2 concentration profile within the particle. In addition to multiplying the computation time, this approach, when employed with a sulfation model, reduced the predicted extent of sulfation of a 50-μm carbonate particle by a factor of 7 below the measured value and by a factor of 5 below the extent calculated if the calcination proceeds by a shrinking-core mechanism on the particle as a whole instead of on the particle grains.

Particle size has been shown to be a controlling factor in the sulfation of both h-CaO and c-CaO (Gullett and Blom, 1987a; Milne, 1988). Figure 13 shows the relationship of surface area and particle diameter for sized carbonates and hydrates. The interdependence of surface area and particle diameter among the stones calcined by Borgwardt (1985) leads one to believe that a more empirical evaluation of Borgwardt's calcination data as a function of initial particle diameter instead of initial surface area should describe the trends in the data.

If the calcination of a carbonate particle proceeds by the shrinking-core mechanism, eq 22 is applicable if r_0 is the initial particle radius instead of the equivalent spherical grain radius based on the BET surface area. By use of the data of Figure 12, a logarithmic plot of the average values of k'/r_0 vs r_0, where r_0 is the particle radius, has a slope of –0.6. If the exponent of r_0 in eq 22 is changed from to

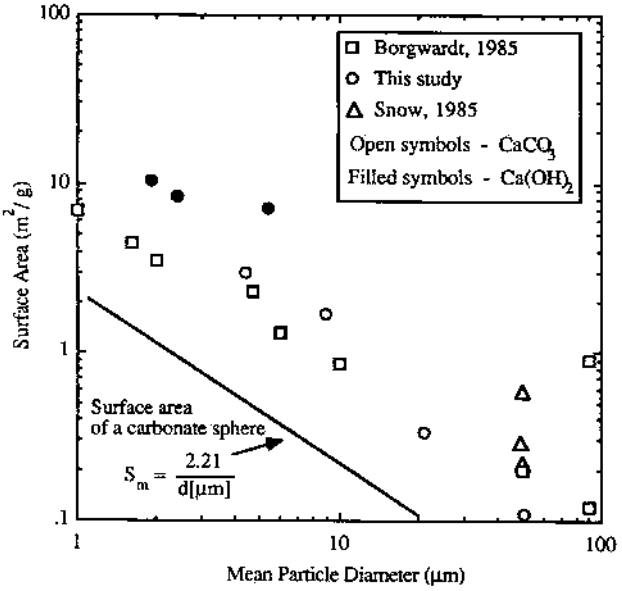

Figure 13. Surface area of sized hydrate and carbonate particles.

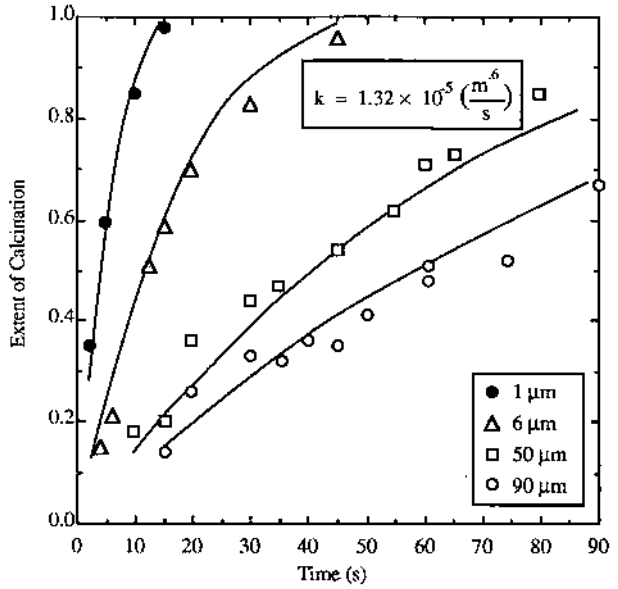

Figure 14. Calcination rate data for sized Georgia marble limestone at 983 K (Borgwardt, 1985) and model fit.

1 to 0.6 and the particle diameter is substituted for the particle radius,

$$x = 1 - \left(1 - \frac{k}{d_0^{0.6}}t\right)^3 \qquad (24)$$

an empirically modified form of the shrinkage-core model at the particle level accurately fits the measured extent of calcination as a function of time and particle size as shown by the curves in Figure 14. Because of its demonstrated applicability to a wide range of particle sizes, eq 24 is employed as the calcination rate equation. This reduced dependence on partricle diameter relative to eq 22 can be partially explained by envisioning that calcination proceeds along a broad reacting front through the particle rather than a distinct reaction interface.

This calcination model not only fits the differential reactor data of Borgwardt, it is consistent with Borgwardt's high-temperature data and other sources of calcination data. Figure 15 shows the calculated rate constants for four separate sets of calcination data obtained from dispersed-phase isothermal reactors. The Borgwardt data and

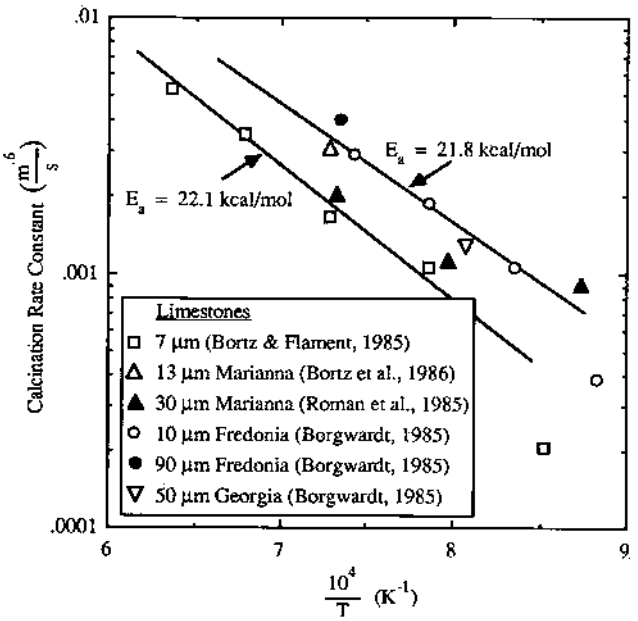

Figure 15. Calcination rate constant plotted as a function of temperature for carbonates of differing particle size and rock source.

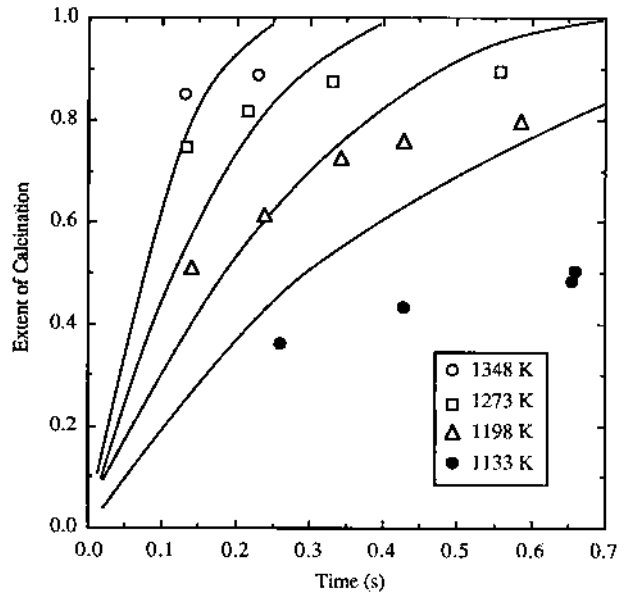

Figure 16. Model fit of Borgwardt (1985) flow reactor calcination rate data for 10-μm Fredenia limestone.

IFRF data of Bortz and Flament (1985) show a change in the activation energy at about 1150 K. Borgwardt's rate constant plot (1985) shows this same trend. Because the high-temperature calcination kinetics are of interest for dry sorbent injection, the data above 1150 K are used to evaluate the calcination rate constant. The IFRF and Borgwardt data have nearly identical activation energies of 22.1 and 21.8 kcal/mol, respectively. The data of Bortz et al. (1985) agree very well with the Borgwardt data. The 7-μm IFRF data have a significantly lower rate constant. Because Borgwardt's data were obtained with particles having narrow size distributions, unlike the other data of Figure 15, the 10-μm high-temperature Borgwardt data, Figure 16, were used to evaluate the carbonate rate constant:

$$k = 10.303 \exp(-10980/T) \qquad (25)$$

Hydrate Rate Equation. The decomposition of $Ca(OH)_2$ is assumed to follow the same mechanism as that for carbonate calcination. Bortz and Flament (1985)

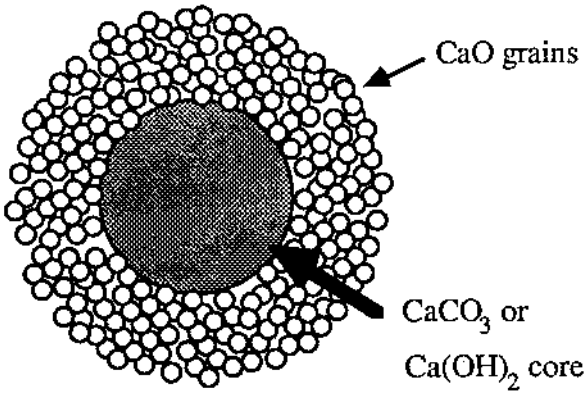

Figure 17. Illustration of the shrinking-core calcination model.

measured 70% calcination after 25 ms at 973 K. The activation energy reported by Mai (1987) and the 973 K data of Bortz and Flament were utilized to estimate the $Ca(OH)_2$ rate constant:

$$k = 53.87 \exp(-8300/T) \qquad (26)$$

For boiler injection temperatures, this rate constant predicts nearly instantaneous calcination.

Particle Model. In harmony with the development of the calcination rate equation, a hydrate or carbonate particle is physically modeled as a sphere, with a measured internal porosity that decomposes by the shrinking-core mechanism. A porous outer shell of high surface area CaO grains is produced, as illustrated in Figure 17. The CaO grains are modeled as overlapping spheres. The porosity of this shell is determined by the theoretical porosity attributed to the parent stone (54% for c-CaO and 49% for h-CaO) and the initial porosity of the sorbent. The initial surface area of small-particle c-CaO generated in a dispersed system is assumed to be 100 m^2/g.

The volume of the reacted parent stone is replaced by concentric shells of uniform overlapping CaO grains. The grains of each shell independently sinter and react with SO_2, where applicable, to simulate ranges of surface area, porosity, and extent of sulfation throughout the particle.

Combined Model

As a check of the combined calcination and sintering model, the surface area and calcination rate data reported by Bortz et al. (1986) of 13-μm Marianna limestone calcined in an isothermal flow reactor at 1373 K are compared to model predictions in Figure 18. The natural gas fired reactor is assumed to have operated at 5% O_2, which serves as a basis for using 7.5 kPa of CO_2 and 14 kPa of H_2O for evaluation of the sintering rate constant. The data suggest an approximate peak surface area of 25 m^2/g at 80% conversion, whereas the model predicts a maximum of 40 m^2/g at 90% conversion. By comparison, Borgwardt (1985) measured an average surface area of 55 m^2/g at 87% conversion for 10-μm Fredonia limestone calcined at 1348 K in a flow reactor with a N_2 atmosphere. Therefore, the model prediction is probably close to the actual surface area of the 13-μm Marianna calcine prior to sample collection where subsequent sintering and recarbonation reduced the surface area to the value measured. The 90% extent of calcination at 0.5 s indicates recarbonation of the sample CaO during sample collection.

Conclusions

The overlapping grain model of Lindner and Simonsson (1981) is consistent with the structure of CaO observed in the SEM photomicrographs. The CaO solid is viewed as a matrix of overlapping spheres that move closer together according to the sintering mechanism of Coble (1958). A sintering rate equation based on the recent experimental data of Borgwardt (1988) is used to calculate the change in surface area of the overlapping grains with time. Extrapolation of surface area and porosity data yields an initial CaO surface area of 100 m^2/g for small-diameter $CaCO_3$ and $Ca(OH)_2$ particles calcined in a dispersed phase. Porosity decreases in direct proportion to the change in surface area per particle volume. The overlapping grain model is confined to coordination numbers of spherical packing of similar porosities. The grain radius and spacing are evaluated by simultaneously solving the nonlinear surface area and volume equations for an overlapping sphere.

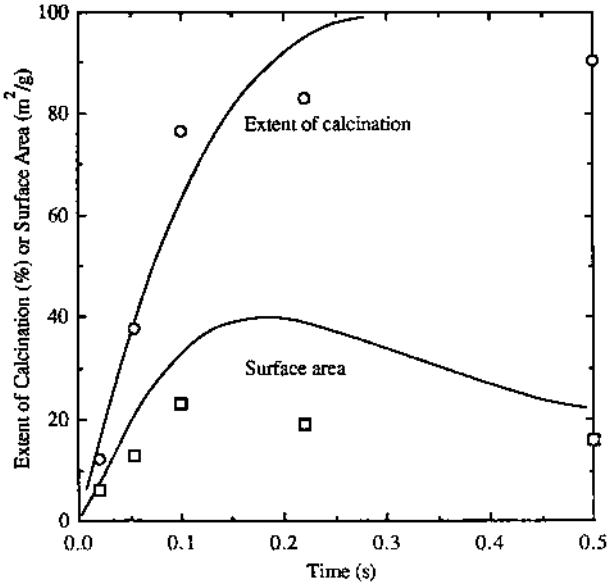

Figure 18. Model predictions for 13-μm Marianna limestone calcined at 1373 K in a flow reactor (Bortz et al., 1986).

The calcination of carbonate or hydrate particles is modeled by the shrinking-core mechanism where a shell of 100 m^2/g overlapping CaO grains is produced as the reaction interface recedes. The calcination rate equation is an empirically modified form of the shrinking-core model with a particle diameter dependence of $1/d_0^{0.6}$. This equation more accurately correlates available high-temperature carbonate calcination data than the more fundamental shrinking-core model applied to individual sorbent grains in the particle.

The combined calcination and sintering model approximates high-temperature observations to within the accuracy of the data, which are extremely difficult to obtain without altering the properties of the dispersed-phase solid. The model simulates the transient high surface area CaO produced upon injection of $CaCO_3$ or $Ca(OH)_2$ particles into a high-temperature gas stream. This transient, highly reactive CaO is of primary interest in the area of dry sorbent injection for SO_2 capture in coal-fired utility boilers. To calcination and sintering models are designed as submodels for a comprehensive sulfation model.

Acknowledgment

The authors gratefully acknowledge the U.S. EPA's extensive financial support and continuing technical assistance throughout the duration of the project. This work was also sponsored in part by the Advanced Combustion Engineering Research Center. Funds for this Center are received from the National Science Foundation, the state

of Utah, 25 industrial participates, and the U.S. Department of Energy.

Nomenclature

d = particle diameter, m
d_0 = initial particle diameter, m
E_a = activation energy, kcal/mol
k' = shrinking-core model calcination rate constant, kg/(m^2 s)
k = calcination rate constant, m$^{0.6}$/s
m = ratio of S to ϵ, m^{-1}
n = coordination number
N = CaO grain number density, m^{-3}
p_i = partial pressure of gas i, kPa
r = CaO grain radius, m
r_c = unreacted particle core radius, m
r_0 = initial sorbent grain or particle radius, m
r_i = CaO grain interface radius, m
R_0 = initial value of the ratio of r_i to r
S = surface area per particle volume, m^{-1}
S_g = surface area of overlapping grain, m^2
S_m = specific surface area, m^2/kg
S_{m0} = initial specific surface area, m^2/kg
S_o = surface area of the overlapped portion of a sphere, m^2
t = time, s
T = temperature, K
V_g = volume of overlapping grain, m^3
V_o = volume of the overlapped portion of a sphere, m^3
V_c = volume of the unreacted sorbent core, m^3
x = extent of calcination

Greek Symbols

ϵ = porosity (void fraction)
ρ = solid density, kg/m^3

Registry No. $CaCO_3$, 471-34-1; $Ca(OH)_2$, 1305-62-0; CaO, 1305-78-8.

Literature Cited

Beruto, D.; Barco, L.; Searcy, A. W.; Spinolo, G. Characterization of the Porous CaO Particles Formed by Decomposition of $CaCO_3$ and $Ca(OH)_2$ in Vacuum. *J. Am. Ceram. Soc.* **1980**, *63*, 439–443.

Bhatia, S. K.; Perlmutter, D. D. A Random Pore Model for Fluid-Solid Reactions: I. Isothermal, Kinetic Control. *AIChE J.* **1980**, *26*, 379–386.

Bhatia, S. K.; Perlmutter, D. D. Effect of the Product Layer on the Kinetics of the CO_2-Lime Reaction. *AIChE J.* **1983**, *29*, 79–86.

Borgwardt, R. H. Calcination Kinetics and Surface Area of Dispersed Limestone Particles. *AIChE J.* **1985**, *31*, 103–111.

Borgwardt, R. H. CaO Sintering in Atmospheres Containing H_2O and CO_2. EPA Paper AEERL-P-398; Air and Energy Engineering Research Laboratory, U.S. Environmental Protection Agency: Research Triangle Park, NC, May 3, 1988.

Borgwardt, R. H. Sintering of Nascent Calcium Oxide. *Chem. Eng. Sci.* **1989**, *44* (1), 53–60.

Borgwardt, R. H.; Harvey, R. D. Properties of Carbonate Rocks Related to SO_2 Reactivity. *Environ. Sci. Technol.* **1972**, *6*, 350–360.

Borgwardt, R. H.; Bruce, K. R.; Blake, J. EPA Experimental Studies of the Mechanisms of Sulfur Capture by Limestone. *Proc. 1st Joint Symp. Dry SO_2 Simul. SO_2/NO_x Control Technol.* July **1985**, *1* (July), EPA-600/9-85-020a (NTIS PB85-232353).

Borgwardt, R. H.; Roache, N. F.; Bruce, K. R. Method for Variations of Grain Size in Studies of Gas-Solid Reactions Involving CaO. *Ind. Eng. Chem. Fundam.* **1986**, *25*, 165–169.

Bortz, S. J.; Flament, P. Recent IFRF Fundamental and Pilot Scale Studies on the Direct Sorbent Injection Process. *Proc. 1st Joint Symp. Dry SO_2 Simul. SO_2/NO_x Control Technol.* **1985**, *1* (July), 17–1, EPA-600/9-85-020a (NTIS PB85-232353).

Bortz, S. J.; Roman, V. P.; Yang, R. J.; Flament, P.; Offen, G. R. Precalcination and Its Effect on Sorbent Utilization During Upper Furnace Injection. *Proc. 1986 Joint Symp. Dry SO_2 Simul. SO_2/NO_x Control Technol.* **1986**, *1* (Oct), EPA-600/9-85-029a (NTIS PB87-120465).

Bruce, K. R.; Gullett, B. K.; Beach, L. O. Comparative SO_2 Reactivity of CaO Derived from $CaCO_3$ and $Ca(OH)_2$. Presented at the Utah LIMB Fundamentals Meeting, Salt Lake City, UT, Dec 14–15, 1987.

Coble, R. L. Initial Sintering of Alumina and Hematite. *J. Am. Ceram. Soc.* **1958**, *41*, 55–62.

Coble, R. L. Sintering Crystalline Solids. II. Experimental Test of Diffusion Models in Powder Compacts. *J. Appl. Phys.* **1961**, *32*, 793–799.

Daniels, F.; Alberty, R. A. *Physical Chemistry*; Wiley: New York, 1975.

Eves, H. Geometry. In *CRC Handbook of Mathematical Sciences*, 5th ed.; Beyer, W. H., Ed.; CRC Press: West Bay, FL, 1978; p 197.

Fischer, H. C. Calcination of Calcite: I. Effect of Heating Rate and Temperature on Bulk Density of Calcium Oxide. *J. Am. Ceram. Soc.* **1955a**, *38*, 245–251.

Fischer, H. C. Calcination of Calcite: II. Size and Growth Rate of Calcium Oxide Crystallites. *J. Am. Ceram. Soc.* **1955b**, *38*, 284–288.

German, R. M.; Munir, Z. A. Surface Area Reduction During Isothermal Sintering. *J. Am. Ceram. Soc.* **1976**, *59*, 379–383.

Gullett, B. K.; Blom, J. A. Calcium Hydroxide and Calcium Carbonate Particle Size Effects on Reactivity with Sulfur Dioxide. *React. Solids* **1987a**, *3*, 337–350.

Gullett, B. K.; Blom, J. A. Porosity, Particle Size, and Surface Area Effects of CaO Reacting with SO_2 at 1100 °C. Utah LIMB Fundamentals Meeting, Salt Lake City, UT, Dec 14–15, 1987b.

Gullet, B. K.; Bruce, K. R. Pore Distribution Changes of Calcium-Based Sorbents Reacting with Sulfur Dioxide. *AIChE J.* **1987**, *33*, 1719–1726.

Haughey, D. P.; Beveridge, G. S. G. Structural Properties of Packed Beds—A Review. *Can. J. Chem. Eng.* **1969**, *47*, 130–140.

Kingery, W. D.; Berg, M. Study of the Initial Stages of Sintering Solids by Viscous Flow, Evaporation-Condensation, and Self-Diffusion. *J. Appl. Phys.* **1955**, *26*, 1205–1212.

Lindgren, E. R. Fuel Rich Sulfur Capture. Ph.D. Thesis, The University of Utah, Salt Lake City, 1988.

Lindner, B.; Simonsson, D. Comparison of Structural Models for Gas-Solid Reactions in Porous Solids Undergoing Structural Changes. *Chem. Eng. Sci.* **1981**, *36*, 1519–1527.

Mai, M. C. Analysis of Simultaneous Calcination, Sintering and Sulfation of Calcium Hydroxide under Furnace Sorbent Injection Conditions. Ph.D. Thesis, The University of Texas, Austin, 1987.

Milne, C. R. High-Temperature, Short-Time Sulfation of Calcium Based Sorbents. Ph.D. Thesis, The University of Utah, Salt Lake City, 1988.

Newton, G. W. Sulfation of Limestone in a Combustion Environment. Ph.D. Thesis, The University of Utah, Salt Lake City, 1987.

Nicholson, D. Variation of Surface Area During the Thermal Decomposition of Solids. *Trans. Faraday Soc.* **1965**, *61*, 990–998.

Ramachandran, P. A.; Doraiswamy, L. K. Modeling of Noncatalytic Gas–Solid Reactions. *AIChE J.* **1982**, *28*, 881–900.

Roman, V. P.; Muzio, L. J.; McElroy, M. W.; Bowers, K. W.; Gallaspy, D. T. Flow Reactor Study of Calcination and Sulfation. *Proc. 1st Joint Symp. Dry SO_2 Simul. SO_2/NO_x Control Technol.* **1985**, *1* (July), EPA-600/9-85-020a (NTIS PB85-232353).

Satterfield, C. N.; Feakes, F. Kinetics of the Thermal Decomposition of Calcium Carbonate. *AIChE J.* **1959**, *5*, 115–122.

Silcox, G. D.; Kramlich, J. C.; Pershing, D. W. A Mathematical Model for the Flash Calcination of Dispersed $CaCO_3$ and $Ca(OH)_2$ Particles. *Ind. Eng. Chem. Res.* **1989**, *28*, 155–160.

Smith, J. M. *Chemical Engineering Kinetics*, 3rd ed.; McGraw-Hill: New York, 1981; p 647.

Snow, M. J. H. The Sulfation of Limestone and Calcium Oxide: Direct and Series Reaction. M.S. Thesis, Massachusetts Institute of Technology, Cambridge, 1985.

Snow, M. J. H.; Longwell, J. P.; Sarofim, A. F. Direct sulfation of Calcium Carbonate. *Ind. Eng. Chem. Res.* **1988**, *27*, 268–273.

Szekely, J.; Evans, J. W.; Sohn, H. Y. *Gas–Solid Reactions*; Academic Press: New York, 1976.

Ulerich, E. P.; O'Neill, E. P.; Keairns, D. L. A Thermogravimetric Study of the Effect of Pore Volume-Pore Size Distribution on the Sulfation of Calcined Limestone. Thermochim. *Acta* **1978**, *26*, 269–282.

Received for review September 6, 1988
Revised manuscript received September 29, 1989
Accepted October 16, 1989